C), we introduced the pairing potential terms $\Delta\psi_{k\uparrow}\psi_{-k\downarrow} + h.c.$ into $H(\mathbf{k})$ and solved the self-consistent mean field gap equation [section 6 of (*16*); *h.c.*, hermitian conjugate]. The in-plane B_{c2} for a sample with a given T_c can then be determined by including the intrinsic SOC term β_{SO} and the Rashba energy $\alpha_R k_F$, where k_F is the Fermi momentum.

For the most extensive data set from sample D1 [$T_c(0)$ = 2.37 K], the relationship between B_{c2}/B_p and the reduced temperature T/T_c, shown in Fig. 4E, can be fitted well with β_{SO} = 6.2 meV and $\alpha_R k_F$ = 0.88 meV. The value obtained for β_{SO} corresponds to an out-of-plane field of ~114 T, which is comparable to the value expected from theoretical calculation at the *K* point (3 meV) (*23*). The Rashba energy obtained can be regarded as an upper bound, because the present model does not include impurity scattering, which can also reduce B_{c2} (*45*).

The scale of B_{c2} enhancement is determined by a destructive interplay between intrinsic β_{SO} and $\alpha_R k_F$. Reaching higher $T_c(0)$ requires stronger doping under higher electric fields, with a concomitant increase of $\mathbf{B}_{Ra}$. As a result of this competition, the in-plane B_{c2} protection should be weakened with the increase of $T_c(0)$. To support this argument, we chose two other superconducting samples that showed consecutively higher $T_c(0)$ (from D1 and D24). By assuming identical β_{SO} (6.2 meV), B_{c2} from D1 with $T_c(0)$ = 5.5 K and B_{c2} from D24 with $T_c(0)$ = 7.38 K can be well fitted using $\alpha_R k_F$ = 1.94 and 3.02 meV, respectively; these values are consistent with the expected increase of $\alpha_R k_F$ with $T_c(0)$ (Fig. 4E).

The effective Zeeman field and its orthogonal protection in individual layers can also be induced by reducing the interlayer coupling in bulk superconducting TMDs (*33*, *35*, *38*, *46*, *47*). Therefore, a large in-plane B_{c2} was also observed in bulk when lattice symmetry was lowered by intercalating organic molecules and alkali elements with large radii (Cs-intercalated MoS_2 shows the highest B_{c2} among bulk phases in Fig. 3D) or by forming a charge density wave (*46*).

We compared our B_{c2} results with those obtained from other superconductors with enhanced B_{c2} under their maximum spin protection along the labeled crystal axis (Fig. 4F); we found that the Zeeman field–protected states in our samples are among the states that are most robust against external magnetic fields. Given the very similar band structures found in 2*H*-type TMDs with universal Zeeman-type spin splitting and the recent successes in inducing more TMD superconductors using the field effect (*17*, *48*, *49*), we would expect a family of Ising superconductors in 2*H*-type TMDs. The concept of the Ising superconductor is also applicable to other layered systems, where similar intrinsic SOC could be induced by symmetry breaking.

REFERENCES AND NOTES

1. G. R. Stewart, *Rev. Mod. Phys.* **56**, 755–787 (1984).
2. M. Tinkham, *Introduction to Superconductivity* (McGraw-Hill, 1996).
3. A. M. Clogston, *Phys. Rev. Lett.* **9**, 266–267 (1962).
4. B. S. Chandrasekhar, *Appl. Phys. Lett.* **1**, 7 (1962).
5. Y. Matsuda, H. Shimahara, *J. Phys. Soc. Jpn.* **76**, 051005 (2007).
6. D. Aoki *et al.*, *Nature* **413**, 613–616 (2001).
7. N. T. Huy *et al.*, *Phys. Rev. Lett.* **99**, 067006 (2007).
8. D. Aoki, J. Flouquet, *J. Phys. Soc. Jpn.* **81**, 011003 (2012).
9. E. Bauer, M. Sigrist, Eds., *Non-Centrosymmetric Superconductors* (Springer-Verlag, 2012).
10. L. P. Gor'kov, E. I. Rashba, *Phys. Rev. Lett.* **87**, 037004 (2001).
11. A. A. Abrikosov, L. P. Gor'kov, *Sov. Phys. JETP* **15**, 752 (1962).
12. R. A. Klemm, A. Luther, M. R. Beasley, *Phys. Rev. B* **12**, 877–891 (1975).
13. P. M. Tedrow, R. Meservey, *Phys. Rev. B* **25**, 171–178 (1982).
14. X. S. Wu, P. W. Adams, Y. Yang, R. L. McCarley, *Phys. Rev. Lett.* **96**, 127002 (2006).
15. R. A. Klemm, *Layered Superconductors: Volume 1* (International Series of Monographs on Physics 153, Oxford Univ. Press, 2011).
16. Materials and methods are available as supplementary materials on *Science* Online.
17. J. T. Ye *et al.*, *Science* **338**, 1193–1196 (2012).
18. K. Ueno *et al.*, *Nat. Mater.* **7**, 855–858 (2008).
19. H. Yuan *et al.*, *Adv. Funct. Mater.* **19**, 1046–1053 (2009).
20. J. T. Ye *et al.*, *Nat. Mater.* **9**, 125–128 (2010).
21. K. Ueno *et al.*, *Nat. Nanotechnol.* **6**, 408–412 (2011).
22. J. Ye *et al.*, *Proc. Natl. Acad. Sci. U.S.A.* **108**, 13002–13006 (2011).
23. A. Kormányos *et al.*, *Phys. Rev. B* **88**, 045416 (2013).
24. N. F. Q. Yuan, K. F. Mak, K. T. Law, *Phys. Rev. Lett.* **113**, 097001 (2014).
25. M. Rösner, S. Haas, T. O. Wehling, *Phys. Rev. B* **90**, 245105 (2014).
26. R. Roldán, E. Cappelluti, F. Guinea, *Phys. Rev. B* **88**, 054515 (2013).
27. T. Eknapakul *et al.*, *Nano Lett.* **14**, 1312–1316 (2014).
28. Y. Zhang *et al.*, *Nat. Nanotechnol.* **9**, 111–115 (2014).
29. Y. Ge, A. Y. Liu, *Phys. Rev. B* **87**, 241408 (2013).
30. M. Tinkham, *Phys. Rev.* **129**, 2413–2422 (1963).
31. N. Reyren *et al.*, *Appl. Phys. Lett.* **94**, 112506 (2009).
32. K. Ueno *et al.*, *Phys. Rev. B* **89**, 020508 (2014).
33. R. A. Klemm, *Physica C* **514**, 86–94 (2015).
34. L. Wang, M. W. Wu, *Phys. Lett. A* **378**, 1336–1340 (2014).
35. R. C. Morris, R. V. Coleman, *Phys. Rev. B* **7**, 991–1001 (1973).
36. R. V. Coleman, G. K. Eiserman, S. J. Hillenius, A. T. Mitchell, J. L. Vicent, *Phys. Rev. B* **27**, 125–139 (1983).
37. D. E. Prober, R. E. Schwall, M. R. Beasley, *Phys. Rev. B* **21**, 2717–2733 (1980).
38. P. Samuely *et al.*, *Physica C* **369**, 61–67 (2002).
39. J. Kačmarčík *et al.*, *Physica C* **468**, 543–546 (2008).
40. R. N. Lyubovskaya, R. B. Lyubovskii, M. K. Kakova, S. I. Pesotskii, *JETP Lett.* **51**, 361 (1990).
41. J. A. Woollam, R. B. Somoano, *Phys. Rev. B* **13**, 3843–3853 (1976).
42. D. Xiao, G.-B. Liu, W. Feng, X. Xu, W. Yao, *Phys. Rev. Lett.* **108**, 196802 (2012).
43. Z. Y. Zhu, Y. C. Cheng, U. Schwingenschlögl, *Phys. Rev. B* **84**, 153402 (2011).
44. H. Yuan *et al.*, *Nat. Phys.* **9**, 563–569 (2013).
45. L. N. Bulaevskii, A. A. Guseinov, A. I. Rusinov, *Sov. Phys. JETP* **44**, 1243 (1976).
46. S. Foner, E. J. McNiff Jr., *Phys. Lett. A* **45**, 429–430 (1973).
47. Y. Kashihara, A. Nishida, H. Yoshioka, *J. Phys. Soc. Jpn.* **46**, 1112–1118 (1979).
48. K. Taniguchi, A. Matsumoto, H. Shimotani, H. Takagi, *Appl. Phys. Lett.* **101**, 042603 (2012).
49. W. Shi *et al.*, *Sci. Rep.* **5**, 12534 (2015).
50. I. J. Lee, M. J. Naughton, G. M. Danner, P. M. Chaikin, *Phys. Rev. Lett.* **78**, 3555–3558 (1997).
51. I. J. Lee, P. M. Chaikin, M. J. Naughton, *Phys. Rev. B* **62**, R14669–R14672 (2000).
52. P. M. Chaikin, E. I. Chashechkina, I. J. Lee, M. J. Naughton, *J. Phys. Condens. Matter* **10**, 11301–11314 (1998).

ACKNOWLEDGMENTS

We acknowledge support from the High Field Magnet Laboratory Nijmegen (HFML-RU/FOM), a member of the European Magnetic Field Laboratory. J.T.Y. acknowledges funding from the European Research Council (consolidator grant no. 648855 Ig-QPD). U.Z. was supported by the DESCO program (2-Dimensional Electron Systems in Complex Oxides, program no. 149) of the Foundation for Fundamental Research on Matter, which is part of the Netherlands Organization for Scientific Research. K.T.L. and N.F.Q.Y. were supported by the Hong Kong Research Grants Council and the Croucher Foundation through grants HKUST3/CRF/13G, 602813, 605512, and 16303014 and an Innovation Grant.

SUPPLEMENTARY MATERIALS

www.sciencemag.org/content/350/6266/1353/suppl/DC1
Materials and Methods
Figs. S1 to S5
Tables S1 and S2
References (*53*–*65*)

30 March 2015; accepted 21 October 2015
Published online 12 November 2015
10.1126/science.aab2277

ICE SHEETS

Fast retreat of Zachariæ Isstrøm, northeast Greenland

J. Mouginot,[1]* E. Rignot,[1,2] B. Scheuchl,[1] I. Fenty,[2] A. Khazendar,[2] M. Morlighem,[1] A. Buzzi,[1] J. Paden[3]

After 8 years of decay of its ice shelf, Zachariæ Isstrøm, a major glacier of northeast Greenland that holds a 0.5-meter sea-level rise equivalent, entered a phase of accelerated retreat in fall 2012. The acceleration rate of its ice velocity tripled, melting of its residual ice shelf and thinning of its grounded portion doubled, and calving is now occurring at its grounding line. Warmer air and ocean temperatures have caused the glacier to detach from a stabilizing sill and retreat rapidly along a downward-sloping, marine-based bed. Its equal-ice-volume neighbor, Nioghalvfjerdsfjorden, is also melting rapidly but retreating slowly along an upward-sloping bed. The destabilization of this marine-based sector will increase sea-level rise from the Greenland Ice Sheet for decades to come.

Zachariæ Isstrøm (ZI) and Nioghalvfjerdsfjorden glacier (NG), in northeast Greenland, drain a sector 198,380 km^2 in size, or 12% of the Greenland Ice Sheet (*1*). These two glaciers together drain the northeast Greenland ice stream, the only large, dynamic feature that extends continuously deep to the ice sheet interior near Greenland's summit (*2*). This marine-based sector holds a 1.1-m sea-level rise equivalent (*3*) (Fig. 1D).

We constructed a high-resolution bed topography of both glaciers (Fig. 1) using a mass conservation method over grounded ice (*3*) and airborne gravity inversion (*4*) over floating ice.

On ZI, we find that the grounding line in year 1996 (*5*) was positioned 450 m below sea level (bsl), on a previously unknown sill that crosses the entire glacier width. Seaward of the sill, the seafloor drops to 800-m bsl (Fig. 1D). Inland of the sill, the glacier bed remains between 400 and 700 m bsl for 30 km. The bed then rises to reach a ridge at sea level. The ridge is cut across by a 300-m-deep channel that connects with interior regions, where the bed remains 300 m bsl for another 150 km. On NG, the 1996 grounding line was 600 m bsl. We find no sill, and the bed is sloping upward until 45 km inland. Seismic data collected in the 1990s (*6*) indicate that the ice shelf floats on a 900-m bsl cavity. The seafloor rises to 200 m bsl to the east, where the ice front is anchored by islands and ice rises, and 600 m bsl to the north into Dijmphna Sund.

[1]Department of Earth System Science, University of California, Irvine, CA 92697, USA. [2]Jet Propulsion Laboratory, California Institute of Technology, Pasadena, CA 91109-8099, USA. [3]Center for Remote Sensing of Ice Sheets, University of Kansas, Lawrence, KS 66045, USA.
*Corresponding author. E-mail: jmougino@uci.edu

We use Landsat optical imagery (fig. S1) to document the ice-front positions over the past 40 years. ZI ice shelf was stable until 2002–2003, when a large section broke off (*7*) and ice debris cleared from Jøkelbugten fjord. The ice front retreated steadily until late 2012, when the northern and southern floating sections became disconnected. In 2013–2014, the ice-front retreat accelerated markedly and the glacier started to calve at its grounding line. By December 2014, the remaining shelf was 52 km^2 in size, or 95% smaller than in 2002. Meanwhile, the calving front of NG retreated by only a few km between 2002 and 2012 (*7*).

We map the glacier grounding lines from 1992 to 2015 (Fig. 1C and figs. S2 and S3) using differential satellite radar interferometry (DInSAR). The grounding line of ZI retreated by 3.5 km at its center between 1996 and 2010, and 3.5 km between 2011 and 2015 (Fig. 1C). The mean rate of grounding-line retreat therefore quadrupled from 230 m/year to 875 m/year before and after 2011. On NG, the grounding line retreated 1 km between 1992 and 2011 and has remained stable since. The DInSAR observations reveal a downward tilting of the ice-front surface of ZI by 75 cm between 16 to 20 December and 20 to 24 December 2014 in a section 1 km wide by 7 km long (Fig. 1C). We attribute this deformation to a buoyancy-driven rotation of the terminus depressed below flotation and facilitated by the propagation of basal crevasses to the water line (*8*).

We document 40 years of surface velocity using Landsat and SAR instruments (table S1 and fig. S4). The results show that after 25 years of stability, the speed of ZI increased by 50% from 2000 to 2014, with half of that increase taking place after 2012 (Fig. 2). The glacier sped up 125 m/year every year from 2012 to 2015, or three times as fast as between 2000 and 2012. NG exhibited smaller changes: Its speed increased by 8% between 1976 and 2014, with most of the acceleration occurring after 2006. The glacier accelerations are larger than seasonal variations and extend 80 km and 15 km upstream of the 1996 grounding lines of ZI and NG, respectively, indicating that the coastal changes affect a substantial portion of the drainage system (Fig. 2).

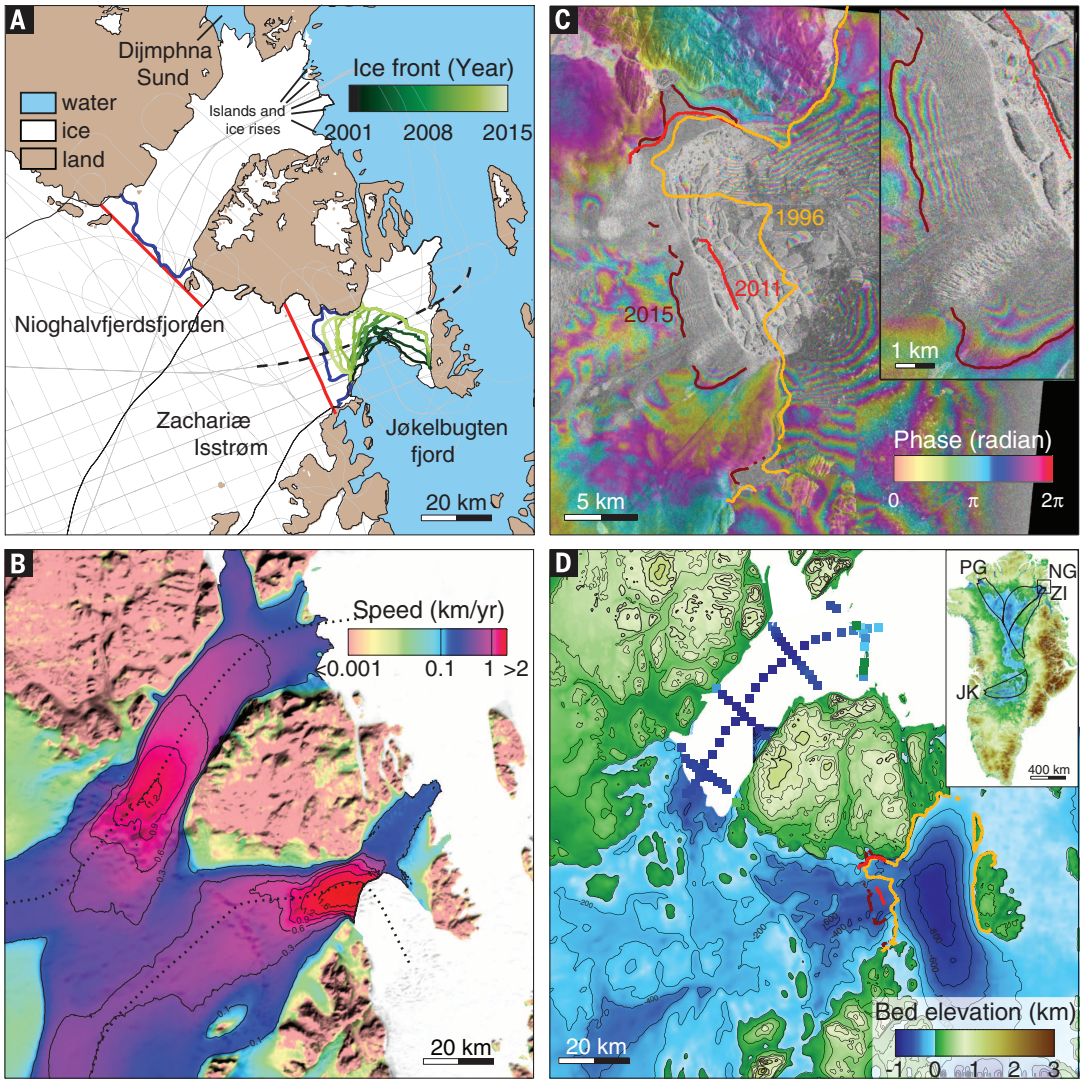

Fig. 1. Ice speed, bed topography, and grounding lines of ZI and NG. (**A**) Schematic view with Operation IceBridge and other NASA mission flight tracks in gray, basin boundaries in black, flux gates in thick blue and red (table S2), and the profile used in Fig. 2 in dashed black. (**B**) Ice surface speed from 2008 to 2009 (*1*), with velocity profiles used in Fig. 3 in black dots. The profiles in (A) and (B) are different. (**C**) Differential interferogram showing the tide-induced motion of ZI in December 2014. The inset shows detail about the pattern of tidal flexure at the grounding line. (**D**) Bed topography above the WGS84 ellipsoid derived from mass conservation on land (*3*) and gravity data at sea (*4*). The seafloor bathymetry beneath NG ice shelf (square) is from seismic measurements (*6*). Inset shows the drainage boundaries of three major marine-based basins in Greenland (*3*).

Repeat measurements of ice thickness (±10-m precision) and surface elevation (±10-cm precision) using radar and light detection and ranging (LIDAR) data (see the supplementary materials) from 1995 to 2014 provide precise information about ice thickness change during the retreat of ZI. About 4.5 km upstream from the 2014 grounding line of ZI, the ice-thinning rate doubled from 2.5 ± 0.1 m/year, consistent with (*9*), to 5.1 ± 0.3 m/year during 1999 to 2010 and 2010 to 2014, respectively. On the ice shelf, the change in ice thickness is large enough to be directly measured with radar (Fig. 3). After correction for dynamic thinning and changes in surface mass balance (SMB), we find that the ice-shelf thickness at the 1996 and 2011 grounding lines decreased by 161 ± 43 m and 100 ± 50 m, respectively, during 1999 to 2010 and 2010 to 2014, reflecting enhanced bottom melting by the ocean of 14.6 ± 4.1 m/year and 25 ± 12 m/year during those time periods (see the supplementary materials). Application of mass conservation on the ice shelf indicated that in the 1990s, the steady-state bottom melt rates of ZI and NG averaged 8 and 5 m/year, respectively, and reached 25 m/year within 10 km of the grounding lines (*5*). We conclude that ice-shelf bottom melting doubled in recent years compared with the 1990s and that half of the increase took place between 2010 and 2014.

On NG, 3.7 km upstream of the 1996 grounding line, ice thinned 0.9 ± 0.1 m/year and 1.4 ± 0.5 m/year during 1999 to 2012 and 2012 to 2014, respectively. The radar echograms show that 5 km downstream of the grounding line, the ice shelf lost 30% of its total thickness (fig. S5). This corresponds to a bottom melting of 13.3 ± 4 m/year in the past 15 years, or 50% above the melt rate from the 1990s (*5*). The ice shelf is therefore eroding rapidly from the bottom. We hypothesize that the erosion has not translated into an inland migration of the grounding line and ice-flow acceleration because the bed of NG rises inland and the ice-shelf front did not detach from bay walls, islands, and ice rises (fig. S5).

Combining surface velocity and ice thickness, we calculate the glacier ice discharge from 1976 to 2015 (Fig. 4 and fig. S6). On ZI, the ice flux increased from 10.3 ± 1.2 Gt/year in 1976 to 15.4 ± 1.7 Gt/year in 2015, or 50%. On NG, the ice discharge increased by 8% from 1976 to 2015. Comparing the ice discharge with net accumulation of mass over the drainage basins (fig. S7) using the regional climate model MAR (Modèle Atmosphérique Régional) (*10*) indicates that ZI was in a state of mass balance until 2003 and is now losing mass at about 5 Gt/year, whereas NG remains close to a state of mass balance (Fig. 4). Our discharge estimates for ZI supersede the overestimates in (*7*) for the period 1990 to 2012, which employed less reliable ice thickness data (figs. S8 and S9).

The MAR reconstruction shows that the mean surface runoff tripled from 0.6 to 1.8 Gt/year, respectively, during 1960 to 1990 and 2002 to 2014 (Fig. 4C) as a result of warmer air temperatures. Higher melting thins ice from the top and contributes to grounding-line retreat as floating ice achieves hydrostatic equilibrium farther upstream. Meltwater ponding on the ice shelf likely contributed to its break-up via hydrofracturing (*11*). Warmer air temperatures melted the ice mélange that keeps ice floes glued together in the fjord (*7*). Enhanced glacier runoff increased subglacial freshwater discharge at the grounding line, which drives a stronger thermohaline circulation at the ice underside and increases the rate of melt by the ocean (*12*).

Ocean in situ measurements over the period 1997 to 2010 show an increase of +1°C in mean temperature of the warm, salty subtropical-origin Atlantic Water (AW) advected from the North Atlantic toward the Arctic Ocean via the West Spitsbergen Current (WSC) (*13*). Although resolving the transport pathways and water-mass transformation of AW in the Northeast Atlantic and East Arctic Ocean is an area of active research (*14*, *15*), it is known that some fraction of these warm northward-flowing waters recirculates in the northern Greenland Sea and in the southern Nansen Basin to join the southward-flowing East Greenland Current (EGC) (*16*). Ocean temperatures observed from moored instruments spanning Fram Strait at 78°50′N from 1997 to the present (*17*) show that temperature anomalies in the northward-flowing WSC also appear in the southward-flowing EGC (*18*). Although high-resolution (2 to 4 km) ocean simulations show that ocean temperature anomalies on the EGC propagate from the continental shelf break into Belgica Trough to within 50 km of ZI (*19*), the seafloor bathymetry in these critical last 50 km is not known well enough to simulate ocean circulation close to the glacier. Yet observations from 1996–1997 (*6*) and 2009 (*20*) reveal the presence of warm AW at the mouth of the NG ice-shelf cavity. A 1°C increase in AW would have increased bottom melting by 10 (*21*) to 20 m/year (*22*), which is within the range of our observations. We conclude that ocean warming most probably played a major role in triggering the glacier retreat, more important than the sea-ice concentration decrease (*7*). Oceanographic observations near ZI are critically needed to address the effect of thermal ocean forcing on the glacier evolution in more detail.

ZI has now transformed into a tidewater glacier calving along an ice cliff as a result of warmer air and ocean temperatures. The mass loss is driven by the increase in ice discharge rather than a change in SMB (Fig. 4). The glacier detached from a stabilizing sill and retreated into a retrograde basin 700 m bsl. Tidewater glaciers are known to retreat rapidly along retrograde beds until the bed rises again (*23*). We project that ZI may continue retreating rapidly for another 20 to 30 years.

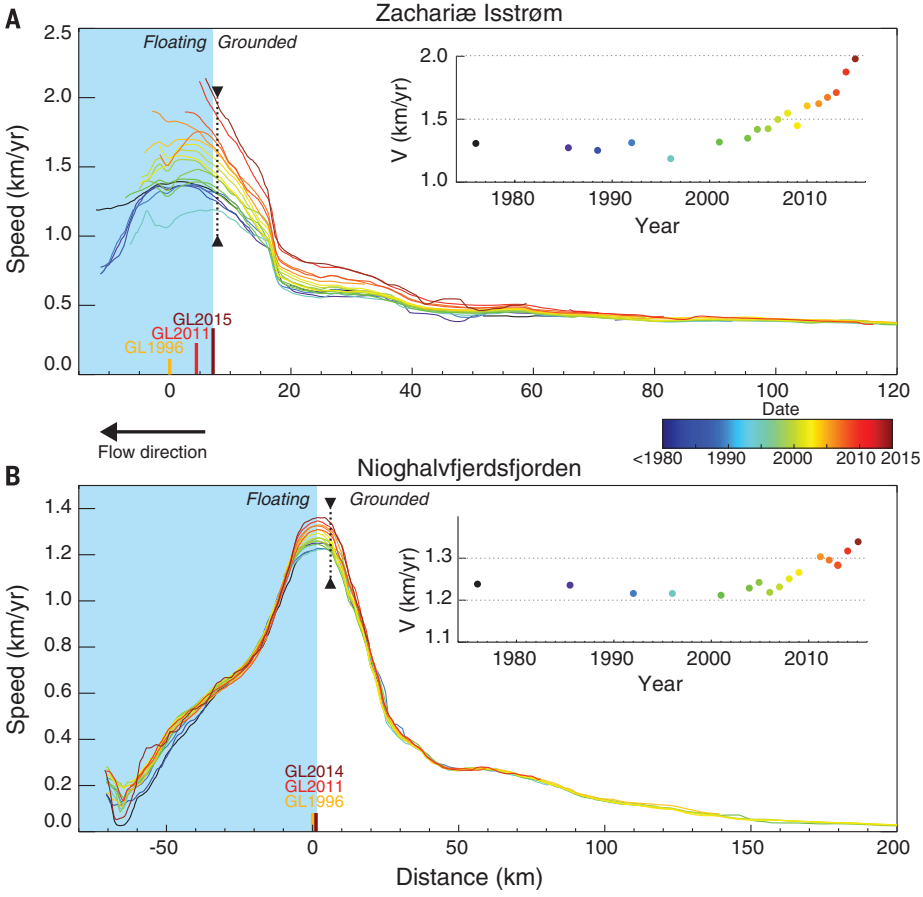

Fig. 2. Ice speed of ZI and NG from 1976 to 2015. (**A** and **B**) Ice speed along the profile in Fig. 1B color-coded from blue (1976) to red (2015). Thick vertical lines locate the grounding lines. The inset displays ice speed versus time at the location of the black dashed vertical line.

Its ice front will progressively widen from 19 km at present to 50 km about 30 km upstream, thereby increasing ice discharge. The height of the calving cliff will increase from its current 75 m to enhance the risk of ice fracture (*11*). With the formation of a calving cliff, the ocean-induced melt rates will increase considerably because buoyant meltwater plumes rise faster along a vertical face than along a near-horizontal ice-shelf bottom (*5*, *12*). Beyond 30 km, the retreat will be slowed down by a rising bed topography, but submarine channels will maintain the contact with the ocean into the deep interior.

The ZI/NG sector is one of three major marine-based basins in Greenland (fig. S10), along with Jakobshavn Isbræ (JI) and Petermann (PG)–Humboldt glaciers, each holding a 0.6-m sea-level equivalent. JI started a rapid retreat (18 km from 2001 to 2015) after the collapse of its ice shelf and has undergone massive calving events since 2010 (*24*) (fig. S11). The central channel of the PG ice shelf lost 250 m of ice from 2002 to 2010, and the ice front retreated 33 km from 2010 to 2012 (*25*). The NG ice shelf will become vulnerable to break-up in the near future if thinning continues. These observations combined suggest that all three major marine-based basins are undergoing substantial changes at present. JI and ZI have already transitioned to a tidewater glacier regime, with increased calf-ice production and ice melting by

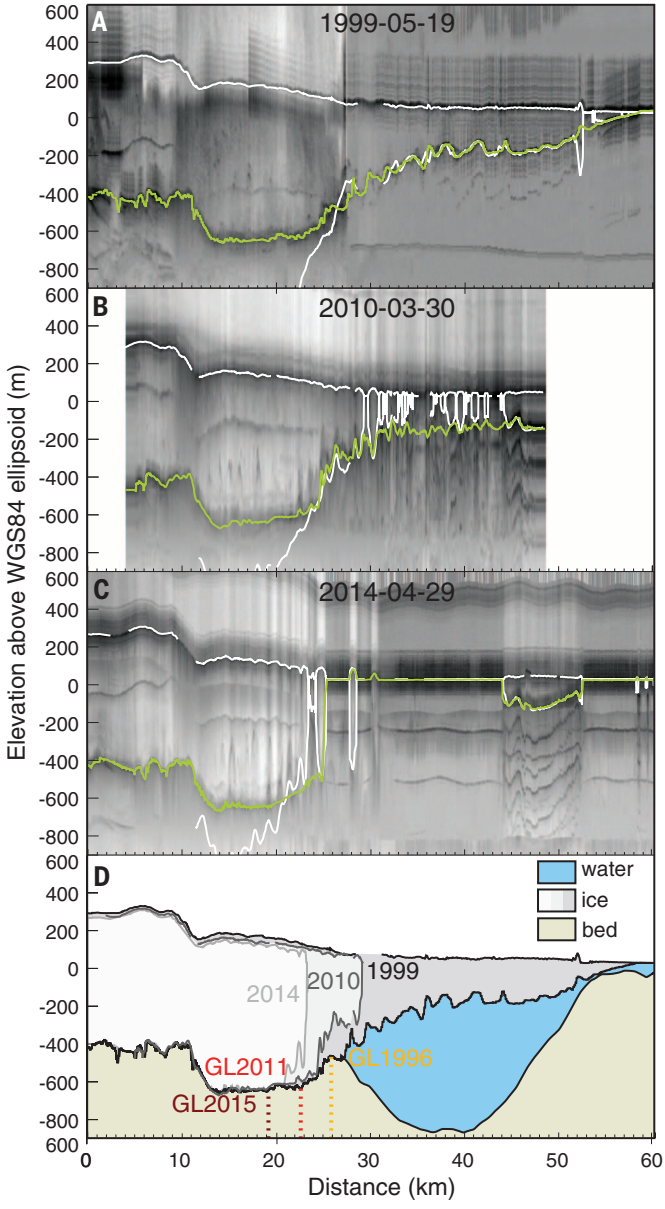

Fig. 3. Surface elevation and ice thickness of ZI from 1999 to 2014. (**A** to **C**) Radar echograms along the center-line profile in Fig. 1A. Ice surface and bottom (assuming flotation) from LiDAR data, respectively, are white. Bed elevation from radar data is green. (**D**) Evolution of ZI between 1999 and 2014, with successive ice-front positions color-coded from dark (1999) to light gray (2014), seawater in blue, and bedrock in light brown. Vertical dashed lines locate the grounding lines.

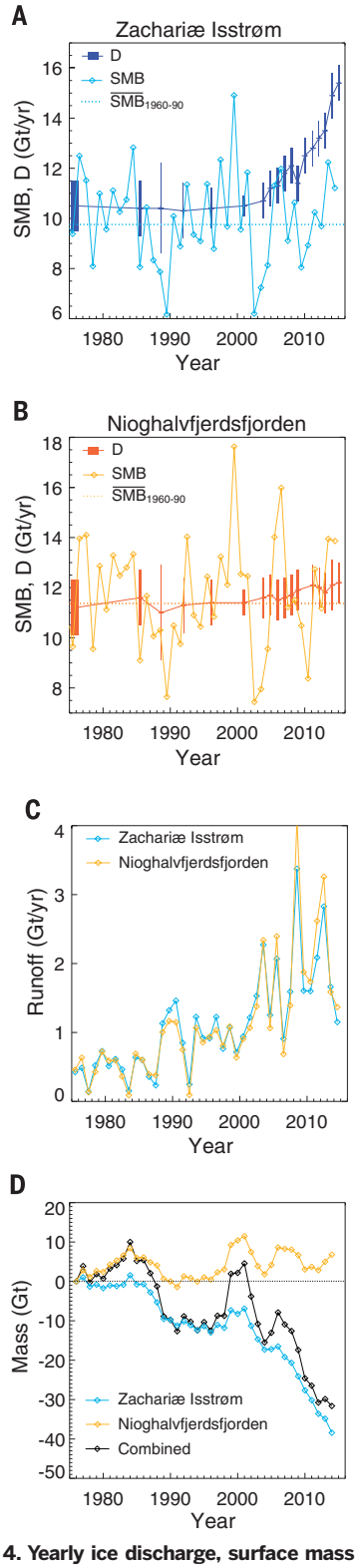

Fig. 4. Yearly ice discharge, surface mass balance, and runoff of ZI and NG from 1976 to 2015. (**A** and **B**) Ice flux [D] and SMB from the regional climate model MAR (*10*) for ZI and NG color-coded blue and orange, respectively. (**C**) Runoff from MAR (*10*). (**D**) Mass evolution of NG, ZI, and both combined. $\overline{SMB}_{1960-90}$ is the mean SMB for the time period 1960–1990.

the ocean. The retreat of these marine-based sectors is likely to increase sea-level rise from Greenland for decades to come.

REFERENCES AND NOTES

1. E. Rignot, J. Mouginot, *Geophys. Res. Lett.* **39**, L11501 (2012).
2. M. Fahnestock, W. Abdalati, I. Joughin, J. Brozena, P. Gogineni, *Science* **294**, 2338–2342 (2001).
3. M. Morlighem, E. Rignot, J. Mouginot, H. Seroussi, E. Larour, *Nat. Geosci.* **7**, 418–422 (2014).
4. J. R. Cochran, R. E. Bell, *J. Glaciol.* **58**, 540–552 (2012).
5. E. Rignot, S. Gogineni, I. Joughin, W. Krabill, *J. Geophys. Res.* **106** (D24), 34007 (2001).
6. C. Mayer, N. Reeh, F. Jung-Rothenhausler, P. Huybrechts, H. Oerter, *Geophys. Res. Lett.* **27**, 2289–2292 (2000).
7. S. A. Khan *et al.*, *Nat. Clim. Change* **4**, 292–299 (2014).
8. T. D. James, T. Murray, N. Selmes, K. Scharrer, M. O'Leary, *Nat. Geosci.* **7**, 593–596 (2014).
9. B. M. Csatho *et al.*, *Proc. Natl. Acad. Sci. U.S.A.* **111**, 18478–18483 (2014).
10. X. Fettweis *et al.*, *The Cryosphere* **7**, 469–489 (2013).
11. D. Pollard, R. M. DeConto, R. B. Alley, *Earth Planet. Sci. Lett.* **412**, 112–121 (2015).
12. Y. Xu, E. Rignot, I. Fenty, D. Menemenlis, M. M. Flexas, *Geophys. Res. Lett.* **40**, 4648–4653 (2013).
13. N. P. Holliday *et al.*, *Geophys. Res. Lett.* **35**, L03614 (2008).
14. K. Orvik, P. Niiler, *Geophys. Res. Lett.* **29**, 1896 (2002).
15. C. Mauritzen *et al.*, *Prog. Oceanogr.* **90**, 62–89 (2011).
16. L. de Steur, E. Hansen, C. Mauritzen, A. Beszczynska-Moeller, E. Fahrbach, *Deep Sea Res. Part I Oceanogr. Res. Pap.* **92**, 26–40 (2014).
17. U. Schauer *et al.*, in *Arctic-Subarctic Ocean Fluxes*, R. R. Dickson, J. Meincke, P. Rhines, Eds. (Springer, Dordrecht, Netherlands, 2008), pp. 65–85.
18. A. Beszczynska-Moeller, E. Fahrbach, U. Schauer, E. Hansen, *ICES J. Mar. Sci.* **69**, 852–863 (2012).
19. E. Rignot, I. Fenty, D. Menemenlis, Y. Xu, *Ann. Glaciol.* **53**, 257–266 (2012).
20. N. J. Wilson, F. Straneo, *Geophys. Res. Lett.* **42**, 7648–7654 (2015). 10.1002/2015GL064944
21. E. Rignot, S. S. Jacobs, *Science* **296**, 2020–2023 (2002).
22. P. R. Holland, A. Jenkins, D. M. Holland, *J. Clim.* **21**, 2558–2572 (2008).
23. M. F. Meier, A. Post, *J. Geophys. Res.* **92** (B9), 9051 (1987).
24. I. Joughin, B. E. Smith, D. E. Shean, D. Floricioiu, *The Cryosphere* **8**, 209–214 (2014).
25. A. Münchow, L. Padman, H. A. Fricker, *J. Glaciol.* **60**, 489–499 (2014).

ACKNOWLEDGMENTS

This work was performed under NASA grants NNX13AI84A (E.R.), NNX14AB93G (E.R.), NNX13AD53A (J.P.), and NNX15AD55G (M.M.), and NSF grant ANT-0424589 (J.P.). The work of I.F., A.K., and E.R. was carried at the Jet Propulsion Laboratory, California Institute of Technology, under a contract with NASA. We gratefully acknowledge European Space Agency, Canadian Space Agency, Japan Aerospace Exploration Agency, Agenzia Spaziale Italiana, National Aeronautics and Space Administration, and Deutsches Zentrum für Luft- und Raumfahrt e.V. for providing SAR data and Polar Space Task Group for coordination of SAR acquisitions.

SUPPLEMENTARY MATERIALS

www.sciencemag.org/content/350/6266/1357/suppl/DC1
Materials and Methods
Supplementary Text
Figs. S1 to S11
Tables S1 and S2
References (*26*–*43*)

10 June 2015; accepted 28 October 2015
Published online 12 November 2015
10.1126/science.aac7111

NEURONAL DYNAMICS

High-speed recording of neural spikes in awake mice and flies with a fluorescent voltage sensor

Yiyang Gong,[1,2,3]* Cheng Huang,[1] Jin Zhong Li,[1,2] Benjamin F. Grewe,[1,2] Yanping Zhang,[1,2,4] Stephan Eismann,[1,2] Mark J. Schnitzer[1,2,4]*

Genetically encoded voltage indicators (GEVIs) are a promising technology for fluorescence readout of millisecond-scale neuronal dynamics. Previous GEVIs had insufficient signaling speed and dynamic range to resolve action potentials in live animals. We coupled fast voltage-sensing domains from a rhodopsin protein to bright fluorophores through resonance energy transfer. The resulting GEVIs are sufficiently bright and fast to report neuronal action potentials and membrane voltage dynamics in awake mice and flies, resolving fast spike trains with 0.2-millisecond timing precision at spike detection error rates orders of magnitude better than previous GEVIs. In vivo imaging revealed sensory-evoked responses, including somatic spiking, dendritic dynamics, and intracellular voltage propagation. These results empower in vivo optical studies of neuronal electrophysiology and coding and motivate further advancements in high-speed microscopy.

To dissect the mechanisms of high-speed neuronal information processing in the live brain, neuroscientists need to track cellular and subcellular electrophysiological activity with millisecond-scale resolution in identified neuron types. Genetically encoded fluorescent Ca^{2+} indicators report isolated, individual action potentials from many cell types in live animals (*1*, *2*). However, Ca^{2+} indicators' slow kinetics (~50 to 1000 ms) precludes high-fidelity studies of fast-spiking cell types, determinations of spike waveforms, resolution of individual spikes in fast spike trains, and precise estimates of spike timing. Moreover, the magnitude of Ca^{2+} influx in response to an action potential varies across cell types and even within individual cells (*1*, *2*). In vivo Ca^{2+} imaging also poorly tracks subthreshold or dendritic voltage dynamics, due to insensitivity to hyperpolarizations and confounds from synaptic Ca^{2+} influx. Organic voltage-sensitive dyes typically have much faster kinetics than Ca^{2+} indicators but are generally highly phototoxic, allow neither genetically targeted delivery nor long-term imaging studies of single cells, and have been incapable of reporting single spikes in the live mammalian brain (*3*).

GEVIs combine genetic targeting and optical readout of transmembrane voltage (*3*, *4*), and in principle can sense spikes and subthreshold dynamics. Nevertheless, to date, GEVIs have lacked the capabilities to detect individual action potentials and fast spike trains in live animals (*3*, *4*).

[1]James H. Clark Center, Stanford University, Stanford, CA 94305, USA. [2]*CNC* Program, Stanford University, Stanford, CA 94305, USA. [3]Department of Biomedical Engineering, Duke University, Durham, NC 27708, USA. [4]Howard Hughes Medical Institute, Stanford University, Stanford, CA, USA.
***Corresponding author. E-mail: yiyang.gong@duke.edu (Y.G.); mschnitz@stanford.edu (M.J.S.)**

Past efforts fused fluorescent proteins to voltage-sensitive domains (VSDs) from voltage-sensitive phosphatases (*5*–*9*) or used Archaerhodopsin (Arch), which is both a fast VSD and a dim fluorophore (*10*). Although Arch variants work well in cultured neurons, the intense illumination required (1 to 10 $W \cdot mm^{-2}$) plus the consequent heating, autofluorescence, and photodamage have precluded imaging studies in intact tissue over wide fields of view (*10*).

Here, we present fast GEVIs (<1-ms response) that fuse the *Acetabularia acetabulum* rhodopsin (Ace) (*11*) and mNeonGreen (*12*) fluorescent protein to enable voltage-sensitive fluorescence resonance energy transfer (FRET) (Fig. 1A and table S1). We previously introduced this "FRET-opsin" configuration (*13*, *14*), which combines the fast kinetics of a rhodopsin VSD with a bright fluorophore and provides high-fidelity membrane potential and spike train readouts at illumination levels ~50 to 100 times lower than those used with Arch indicators. A FRET-opsin indicator based on *Leptosphaeria maculans* (Mac) rhodopsin and yellow fluorescent mCitrine reported fast neural spiking in brain slices and Purkinje neurons' dendritic activation in live mice (*13*). These results had suggested that optical recordings of action potentials and dendritic voltage dynamics in live animals might be attainable. Ace-mNeon indicators now enable high-fidelity imaging of individual spikes and fast spike trains in live mice and flies due to their faster kinetics and superior brightness compared with all prior GEVIs. Ace is about six times as fast as Mac, and mNeonGreen has a ~50% higher extinction coefficient than mCitrine and nearly threefold better photostability (*12*). We created Ace mutants (Ace1Q and Ace2N) with an inactivated proton pump; these have blue-shifted absorption spectra compared with Mac and Arch (*11*, *13*), yielding superior